Volume 12
Number 21
7 November 2025
Pages 8759–9320

Materials Horizons

rsc.li/materials-horizons

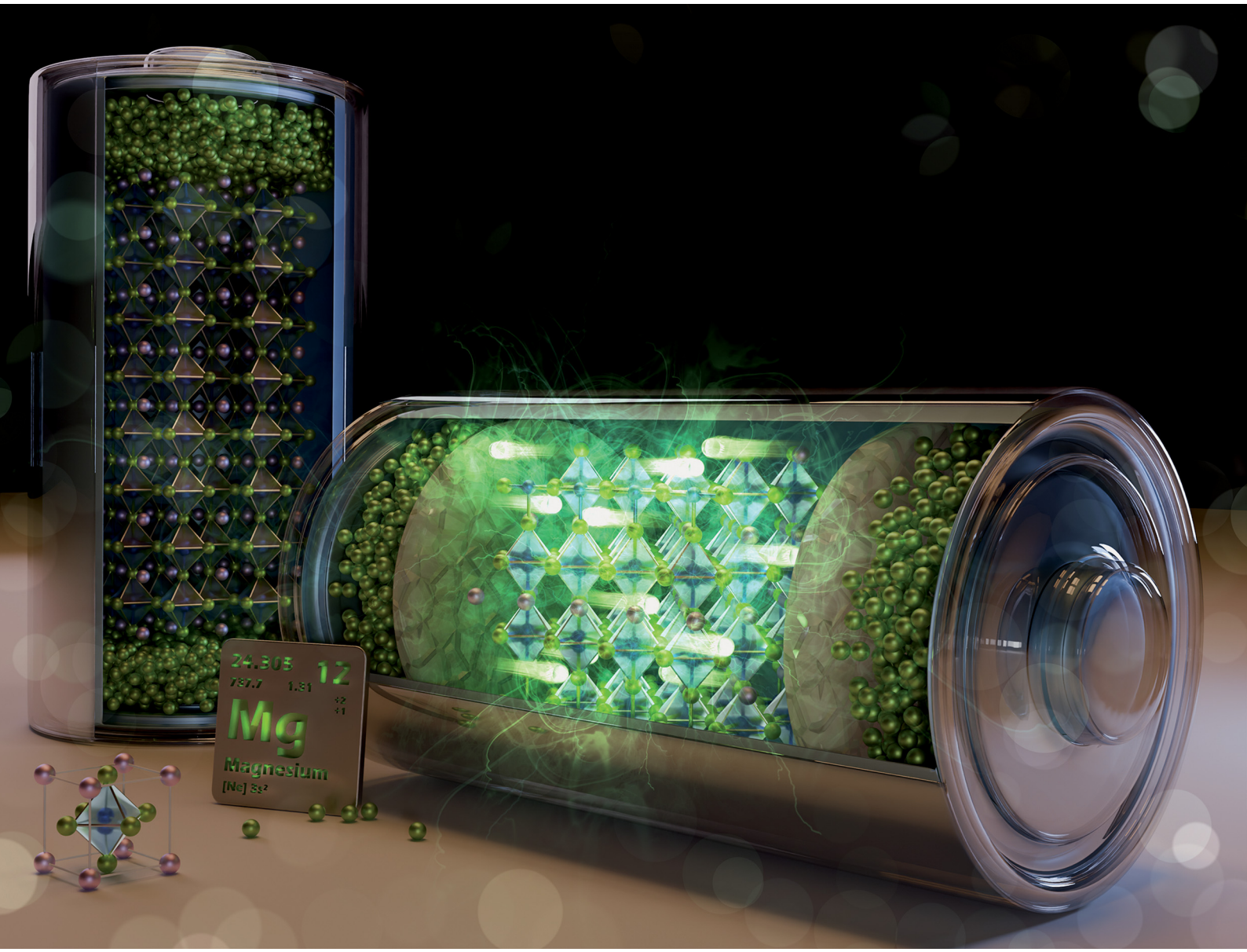

ISSN 2051-6347

ROYAL SOCIETY OF CHEMISTRY

COMMUNICATION
Timo Jacob, Hagar K. Hassan *et al.*
Is Mg_3AsN antiperovskite a promising Mg-ion conductor?

Materials Horizons

ROYAL SOCIETY OF CHEMISTRY

COMMUNICATION

View Article Online
View Journal | View Issue

Cite this: *Mater. Horiz.*, 2025, **12**, 9026

Received 16th July 2025,
Accepted 18th September 2025

DOI: 10.1039/d5mh01361e

rsc.li/materials-horizons

Is Mg_3AsN antiperovskite a promising Mg-ion conductor?

Paul Hoffmann, [a] D. Iván Villalva-Mejorada, [ad] Omar W. Elkhafif, [a] Thomas Diemant, [bc] Timo Jacob *[abc] and Hagar K. Hassan *[abc]

Among solid-state electrolytes (SEs), antiperovskites (APs) with an X_3AB structure stand out as SEs for monovalent-ion batteries due to their inverted perovskite framework, which supports cation-rich compositions with high ionic conductivity. For rechargeable Mg batteries (RMBs), Mg_3AsN was theoretically predicted as a potential Mg-ion conductor. Motivated by conflicting theoretical predictions regarding its electronic properties, which highlight the need for experimental validation, in the present work, we performed the first experimental investigation of the ionic and electronic properties of Mg_3AsN. Mg_3AsN was synthesized by high-energy ball milling and characterized by different structural and electrochemical techniques. Pristine Mg_3AsN exhibited mixed ionic and electronic conductivities of 5.5×10^{-4} S cm^{-1} and 4.89×10^{-8} S cm^{-1}, respectively, at 100 °C. After hot pressing, the electronic conductivity was found to be 1.5×10^{-6} S cm^{-1}. Heat treatment at 600 °C for 12 hours improved the total ion transport number from 0.07 to 0.615, while maintaining the electronic conductivity at 5×10^{-8} S cm^{-1} at 100 °C. To further suppress the electronic conductivity of Mg_3AsN, two approaches were performed: (i) adding electron-blocking buffering layers of metal–organic frameworks between AP and Mg electrodes and (ii) dispersing the AP powder into a polymeric matrix to block electron flow while preserving ion diffusion. Initial results from both strategies were promising and showed enhanced viability of Mg_3AsN as an SE, offering tunable solutions for RMB development and to implement mixed conductors with high ionic conductivity in solid-state batteries (SSBs). A suppressed electronic conductivity, as well as a room temperature ionic conductivity of 0.134 mS cm^{-1}, was achieved, affording a reversible Mg^{2+} deposition/stripping process.

New concepts

This study introduces a ground-breaking experimental validation of Mg_3AsN antiperovskite as a viable solid-state electrolyte (SE) for rechargeable magnesium batteries (RMBs), addressing the critical challenge of slow Mg^{2+} ion diffusion in solid-state systems. Inspired by prior theoretical proposals, we provide the first comprehensive investigation of Mg_3AsN's ionic and electronic properties, revealing its mixed conductivity as a key limitation. By innovatively suppressing its electronic conductivity using electron-blocking matrices, such as metal–organic frameworks or polymers, by two different approaches, we achieve reversible Mg^{2+} deposition and stripping, unlocking Mg_3AsN's potential for RMBs. This breakthrough distinguishes Mg_3AsN from other Mg-ion conductors due to its good ionic conductivity, compatibility with scalable electronic suppression strategies, and simpler synthesis compared to existing SEs. Our work advances materials science by demonstrating a practical approach to overcoming mixed conductivity in antiperovskites, offering new insights into designing efficient, cost-effective, and safe solid-state electrolytes for next-generation batteries.

1. Introduction

Despite magnesium's lower specific capacity and redox potential relative to lithium, its excellent safety profile makes it a promising candidate for replacing Li in certain energy storage applications, particularly those emphasizing safety and long-term stability. However, the current limitations in practical electrolytes and cathodes present significant barriers to the broader adoption of rechargeable magnesium batteries (RMBs).[1,2] The lack of suitable materials for these essential components restricts the transition of promising laboratory discoveries into commercially feasible products. Addressing these obstacles is imperative to fully harness the potential of magnesium in rechargeable metal-ion batteries. One promising avenue for resolution is the development of solid-state electrolytes (SEs), a focal point of cutting-edge research in the battery community due to their anticipated superior performance and safety compared to liquid-based alternatives. Furthermore, SEs offer the opportunity for electrochemical advancements through novel architectural designs.[3] However, due to the high

[a] *Institute of Electrochemistry, Ulm University, Albert-Einstein-Allee 47, 89081, Ulm, Germany. E-mail: timo.jacob@uni-ulm.de, hagar.khalil-hassan@uni-ulm.de*
[b] *Karlsruhe Institute of Technology (KIT), P. O. Box 3640, 76021, Karlsruhe, Germany*
[c] *Helmholtz Institute Ulm (HIU), Electrochemical Energy Storage, Helmholtz Str. 11, 89081, Ulm, Germany*
[d] *Instituto Politécnico Nacional, Laboratorio Nacional de Conversión y Almacenamiento de Energía, CICATA, Calzada Legaria No. 694, Irrigación, CDMX, 11500, México*

charge density of Mg ions, they exhibit sluggish mobility within solid conductors.[4] Therefore, exploring new materials with fast ion-transport properties is highly demanding. Antiperovskites (APs) have recently gained significant attention in solid-state batteries due to their high ionic conductivity and remarkable structure tunability.[5,6] APs, also known as inverted perovskites, belong to a class of materials sharing structural similarities with the widely recognized perovskite structure (ABX_3). However, in antiperovskites, the arrangement and stoichiometry of anions and cations are structurally inverted (X_3BA), which alters their properties.[5,7] Moreover, antiperovskites have the capacity to host a significant number of metal cations within their network. The structure of an antiperovskite can be conceptualized as a cubic cell, with A anions situated at the center, B anions occupying the corners, and X cations positioned at the center of each face. Each B anion is surrounded by six X cations, forming an X_6A octahedron.[5,7] The diffusion of the metal ions inside the crystal lattice of APs can be easily facilitated through chemical manipulations and defect creation.[8] The distinctive structure and properties of APs make them promising candidates for solid electrolytes not only in lithium-ion batteries but also in advanced battery systems beyond lithium technology.[9,10] For instance, Li-ion-rich solid electrolytes known as LRAPs have been identified as promising materials for enhancing the performance of Li-ion batteries.[9] Moreover, altering the composition of these materials, such as substituting ions of different sizes or inducing defects, can lead to structural distortions affecting ion mobility within the material.[5] Zhao and Daemen reported rapid Li-ion conduction in Li_3OX (X = Cl, Br, or mixed halides) solid electrolytes.[9] They demonstrated that the structural configuration significantly influences their ionic conductivity, highlighting the enhancement achieved by doping anion sites in Li_3OCl to create $Li_3OCl_{0.5}Br_{0.5}$, which exhibited an increased ionic conductivity of 1.95 mS cm^{-1}.[11] Similarly, other studies have achieved notable results, such as attaining an ionic conductivity of 25 mS cm^{-1} at room temperature through divalent cation doping of lithium ions in Li_3OCl.[12] This concept has been extended to design Na-ion-rich solid electrolytes (NRAPs), exemplified by Na_3OA (A = BH_4^-, NO_3^-, and CN^-).[10] Similarly, Goldmann *et al.* also found that doping and introducing defects significantly influence the ionic conductivity of NRAPs.[6] Dutra and Dawson achieved an activation energy of 0.12 eV, a room temperature ionic conductivity of 6.3 mS cm^{-1}, and compatibility with sodium metal anodes.[13] Regrettably, to date, there have been only minimal efforts to experimentally engineer solid electrolytes for multivalent ions based on AP structures. However, numerous theoretical studies have identified potential candidates exhibiting promising characteristics as multivalent ionic conductors. Among these studies, a recent investigation by Kim and Siegel delved into the structural, elastic, and electronic properties of cubic solid electrolytes (APs) with the composition Mg_3AN (where A = P, As, Sb, and Bi).[14] Their findings suggested that Mg_3AsN could serve as a rapid conductor for Mg ions. However, several other research endeavors have examined the electronic characteristics of Mg_3AsN, revealing significant disparities in the calculated bandgap values.[15–21] Kim and Siegel's calculations yielded a bandgap of 2.68 eV and predicted its high potential to act as a SE, in contrast to direct bandgap estimates ranging from 1.3 to 2.3 eV in other publications.[7,14–16,22] Consequently, whether Mg_3AsN is a potential SE remains uncertain and needs experimental validation. Therefore, the present work aims at providing an experimental validation of the ionic and electronic properties of Mg_3AsN and correlate these findings with the theoretical studies mentioned above.

2. Experimental

2.1 Materials and chemicals

Magnesium foil (thickness = 0.025 mm, ∅ 12 mm) and copper foil (thickness = 0.0125 mm, ∅ 12 mm) were purchased from Alfa Aesar and were used for symmetric cell assembly. Magnesium nitride (CAS number: 12057-71-5) was purchased from Merck. Arsenic (99.999% trace metals basis, CAS number: 7440-38-2), *N*-dimethylformamide (DMF) (CAS number: 68-12-2), zirconium chloride (CAS number: 10026-11-6), terephthalic acid (BDC) (CAS number: 100-21-0), and HCl (37%) were purchased from Sigma Aldrich. *N*-Methyl-*N*-propylpiperidinium bis(trifluoromethanesulfonyl)imide ([MPPip][TFSI]) (CAS number: 608140-12-1) and 1-ethyl-3-methylimidazolium-bis(trifluoromethylsulfonyl)-imide (EMIM-TFSI) (CAS number:174899-82-2) were purchased from Iolitec. Poly(vinyl alcohol) (PVA) (CAS number: 9002-89-5), poly(ethylene glycol) diacrylate (PEGDA) (CAS number: 26570-48-9), poly(vinylidene fluoride-*co*-hexafluoropropylene) (PVDF-HFP) (CAS number: 9011-17-0), 2,2′-azobis(2-methylpropionitrile) (AIBN) (CAS number: 78-67-1) dissolved in acetone, and *N*-methyl-2-pyrrolidone (NMP) (CAS number: 872-50-4) were purchased from Sigma Aldrich.

All salts and powders were heated at 120 °C under vacuum overnight and stored in an Ar-filled glovebox with O_2 and H_2O levels $\leq$0.5 ppm before further use.

2.2 Material synthesis

2.2.1 Attempts to synthesize Mg_3AsN *via* a high-temperature solid-state reaction. Mg_3AsN was tried to be synthesized *via* a high-temperature solid-state reaction using the method reported by Chi *et al.*[23] Here, arsenic and magnesium nitride were ground together in an argon-filled glovebox. The mixture was pressed into a pellet of ∅ 13 mm under a pressure of 5 tons for one minute. After that, the pellet was loaded into a quartz tube in a vacuum atmosphere and sealed inside the glovebox. The tube was then transferred to a tube furnace and heated at 800 °C for 60 h. Various trials using different ramping rates and heating steps were conducted. For example, the material was initially heated to 400 °C at a ramp rate of 40 °C h^{-1} and held at this temperature for 24 hours. Then, the temperature was increased to 800 °C at a ramp rate of 15 °C h^{-1}, where it was maintained for 60 hours before being naturally cooled to room temperature. In another synthesis, a ramp rate of 40 °C h^{-1} was used to reach 400 °C, where the temperature was held for 10 hours. The ramp rate was then adjusted to 20 °C h^{-1} up to 600 °C, held for 10 hours, and then increased at 20 °C h^{-1} up to 800 °C for another

10 hours before cooling down naturally. Fast heating and cooling rates were also attempted.

2.2.2 Mechanochemical synthesis of Mg_3AsN. Mg_3AsN was synthesized by ball milling (BM) a stoichiometric amount of Mg_3N_2 with arsenic powder in an 80 mL zirconia jar (Fritsch) using 15 (10 mm) and 10 (5 mm) balls at 300 or 400 rpm for 3–24 h (30 minutes on, followed by 15 minutes pause). Prior to ball milling, the precursors were mixed and ground together in the glovebox. The BM jar was sealed inside the glovebox using a special sealing apparatus so that neither the reactants nor the products were exposed to air. After the ball milling process, the as-milled Mg_3AsN was collected inside the glovebox and stored for further use.

2.2.3 Post-heat treatment. The as-ball milled material was subjected to a post-treatment process to improve its crystallinity at different temperatures (300–800 °C in 100 °C increments) for different annealing times (12–20 h). Nearly 0.5 g of as-ball milled Mg_3AsN was pressed in a ∅ 13 mm mold under 5.0 tons for 1.0 min. The pellets were inserted into a large quartz tube and sealed inside the glovebox prior to being heated in a Nabertherm large tube furnace.

2.2.4 Preparation of an electron blocking layer (MOFsSE). Metal–organic framework-based semi-solid electrolytes (MOFsSE) were used as electron-blocking layers. In this work, a UIO-66 metal–organic framework (MOF) was synthesized by a hydrothermal reaction of $ZrCl_4$ with BDC in a DMF solvent.[24] Herein, 0.125 g of $ZrCl_4$ was dissolved in 5.0 mL of DMF and 1 mL of HCl (37%), while 0.123 g of BDC was dissolved in 10 mL of DMF. The two solutions were mixed in a 25 mL Teflon-lined autoclave and heated at 80 °C for 16 h. The resulting solid was collected by centrifugation at 5500 rpm for 10 min and then washed with warm DMF and ethanol three times each. The white product was then dried at 90 °C in a vacuum oven to remove any solvent. Subsequently, 0.4 g of the MOF was ground together with 375 μL of the ionic liquid [MPPip][TFSI] containing 0.1 M $Mg[TFSI]_2$ and 0.01 M $Mg(BH_4)_2$. 0.1 g of the semi-solid electrolyte (sSE) was pressed into a pellet of ∅ 13 mm under a pressure of 7 tons for 3 min. For simplicity, the abbreviation MOFsSE was assigned to this buffering (electron-blocking) layer.

2.2.5 Preparation of a free-standing Mg_3AsN/polymer electrolyte. A free-standing Mg_3AsN–polymer was prepared by dispersing as-ball milled Mg_3AsN in our newly designed co-polymer matrix. The co-polymer matrix is composed of poly(vinyl alcohol) (PVA), poly(ethylene glycol) diacrylate (PEGDA) as a cross-linker, and poly(vinylidene fluoride-*co*-hexafluoropropylene) (PVDF-HFP). 140 mg of PVA was added to 90 mg (80.4 μL) of PEGDA, while the ratio of PVA/PEGDA was maintained at 7 : 4.5. Then, 10 wt% poly(vinylidene fluoride-*co*-hexafluoropropylene) (PVDF-HFP) relative to the total mass of PVA and PEGDA was added. After adding 6 wt% (relative to the PEGDA mass) of a 12% solution of 2,2′-azobis(2-methylpropionitrile) (AIBN) initiator in acetone, along with 0.100 g of Mg_3AsN, EMIM-TFSI ionic liquid (of different ratios ranging from 1 : 1 to 1 : 3 with respect to PVA), and 2 mL of *N*-methyl-2-pyrrolidone (NMP), an anhydrous solvent was introduced into the polymer matrix. Then, the co-polymers were allowed to polymerize by the free radical polymerization reaction (RAFT polymerization) at 60 °C for 6 h under continuous stirring to form a homogenous solution. Later, the blend precursor was cast onto a polytetrafluoroethylene plate and heated under vacuum at 50 °C for 4 h, followed by 80 °C for 8 h. The thickness of the membrane was controlled to be around 100–150 μm.

2.3 Structural, surface, and spectral characterization

X-ray powder diffraction (XRD) patterns were recorded on a STOE Stadi P diffractometer under the following conditions: CuKα radiation (λ = 0.154 nm; 40 kV, 40 mA) in the transmission mode. The powders were assembled in a sample holder inside the glovebox to avoid air exposure and covered by Kapton© tape. X'pert Highscore software (PANalytical) was used for XRD pattern analysis. Rietveld refinement of the structure was performed using FullProf software. The Rietveld refinement method was used to refine the theoretical crystal structure model by minimizing the difference between the observed and calculated XRD patterns and to adjust atomic positions, thermal vibrations, and lattice constants.[25] The scanning electron microscopy (SEM) imaging and energy dispersive X-ray spectroscopy (EDX) measurements were carried out using a Zeiss LEO 1550 VP field emission SEM (FE-SEM Carl Zeiss, Germany). A transfer box was used to transport samples from the glovebox to the SEM chamber without exposure to air. XRD was used to investigate the chemical and air stabilities of the as-synthesized Mg_3AsN after leaving the powders in a fume hood for 3–72 h or dissolving a small amount in different solvents and then leaving them in a fume hood for 24 h, followed by a drying process in air. X-ray photoelectron spectroscopy (XPS) measurements were acquired using a PHI 5800 MultiTechnique ESCA System (Physical Electronics). To avoid surface contamination, the samples were transferred in an inert gas atmosphere to the sample load lock of the XPS system. The spectra were recorded using monochromatized Al K_α (300 W, 15 kV) radiation, a detection angle of 45°, and pass energies at the analyser of 93.9 and 29.35 eV for survey and detail spectra, respectively. The samples were neutralized with electrons from a flood gun to compensate for charging effects at the surface. The main C-1s peak was set to 284.8 eV for binding energy calibration. For a depth profile, the topmost surface layers were removed by successive sputtering (I_{Sp} ∼ 1 μA and U_{Sp} 5 kV) for 2, 4, 6 and finally 8 minutes, resulting in total sputter times of 0, 2, 6, 12 and 20 minutes. According to the instrument manufacturer, the sputter rate should be ∼1 nm min^{-1} under the given conditions. Peak fitting was performed using the CasaXPS software with Shirley-type backgrounds and peak shapes based on the Gaussian–Lorentzian product function (GL30).

2.4 Electrochemical characterization

Electrochemical impedance spectroscopy (EIS) and ionic conductivity measurements were recorded with a Solartron potentiostat. Pellets of MgAPs for the electrochemical measurements were prepared in an Ar-filled glovebox by dispensing 0.2 g of MgAPs between two metal foils and then sandwiching between

two stainless steel discs into a cylindrical PEEK cell of inner diameter 13 mm. The loaded material was then pressed at 5 tons for one minute before the thickness measurements using a thickness gauge accurate to 0.2 μm. The thickness of the formed pellets was between 0.62 and 0.69 mm. Before the electrochemical tests, the inner PEEK cell with the MgAP pellet was hosted in a stainless-steel case with an upper screw applying a force to the upper part to ensure the cell's electrical contact and stable mechanical stability. The whole cell was further sealed to avoid any possible exposure to air.

2.4.1 Ionic and electronic conductivity measurements of Mg_3AsN. Before EIS measurements, the cells were sintered at 100 °C for two days. Electrochemical impedance spectroscopy was used for the conductivity measurements at a temperature ranging from 40 to 100 °C, where the cells were kept at each temperature for two hours before the measurement. All of the data were collected at an amplitude of 40 mV in the frequency range between 1.0 MHz and 100 mHz, with 100 points per measurement. Before cell assembly, the pellets were Au-coated from both sides inside the glovebox by using a Q150 GB sputter coater from Quorum Technologies.

Deconvolution of the ionic and electronic conductivities was achieved by three parallel experiments. First, the EIS spectra of Mg_3AsN sandwiched between two ion-blocking electrodes (iBE, ion-blocking electrode = Au or Cu) were recorded. Second, the electronic conductivity of Mg_3AsN was determined by chronoamperometry (CA), measuring the polarization of an iBE|Mg_3AsN|iBE cell at various applied potentials (0.5–3.0 V), and then recording the change in current with time until steady-state current was achieved. The applied potential was then plotted against the steady-state current, and the electronic resistance was calculated from the slope using Ohm's law. The third experiment involved the EIS recording of an electron-blocking cell configuration. Herein, two MgMOFsSE buffering layers were used as electron blocking electrodes (eBE) in a Mg|eBE|Mg_3AsN|eBE|Mg cell configuration, which enables ionic conduction only and hinders electronic conduction. In this case, the obtained bulk resistance is the sum of the bulk resistances of eBE (MOFsSE) and that of Mg_3AsN. By knowing the bulk conductivity of eBE, the ionic conductivity of Mg_3AsN can be calculated following the methodology reported by Glaser *et al.* in 2023.[26] After calculating the values of ionic and electronic conductivities of Mg_3AsN, equivalent circuit fitting of EIS results of an iBE|Mg_3AsN|iBE cell was used to double-check and confirm the deconvolution.

The ionic resistance was calculated by fitting the Nyquist plot using the ZView software from Scribner, LLC. Then, the ionic conductivity was calculated using eqn (1),

$$\sigma = \frac{l}{R_b A} \tag{1}$$

The pseudo-activation energies were then calculated using eqn (2),[27]

$$\sigma = \sigma_0 \cdot e^{-\frac{E_a}{k_B T}}, \tag{2}$$

where σ is the bulk conductivity in S cm^{-1}, l is the pellet thickness in cm, R_b is the bulk resistance in ohms, A is the pellet area in cm^2, σ_0 is the pre-exponential factor, T is the absolute temperature in kelvin, E_a is the pseudo-activation energy of diffusion, and k_B is the Boltzmann constant.

For total transport number calculations, SE pellets were sandwiched between two iBEs (Cu foils, ∅ 13 mm or sputtered Au layer pellets, thickness 100 nm) before applying a DC potential of 0.5 V for 2–3 hours until a steady-state current was achieved. The total ion transport was then calculated using eqn (3),

$$t_{ion} = \frac{I_0 - I_s}{I_0} \tag{3}$$

where I_0 is the initial current (at $t = 0$), I_s is the steady-state current, and t_{ion} is the total ion transport number.

3. Results and discussion

3.1 Synthesis and characterization

In 2002, Chi *et al.*[23] reported a method to synthesize both Mg_3AsN and Mg_3SbN by a high-temperature solid-state reaction at 800 °C. However, our trials to reproduce this synthesis were unsuccessful. We observed the evaporation of the arsenic metal during the heating process, resulting in a high percentage of unreacted Mg_3N (see Fig. S1) and arsenic residues on the walls of the quartz tube. As mentioned in the Experimental section, various trials using different ramping rates and heating steps were attempted, but none of these trials yielded successful results. It should be noted that we were unable to find any evidence of the successful synthesis of Mg_3AsN in the work by Chi *et al.*;[23] only the synthesis of Mg_3SbN was demonstrated. On the other hand, as identified by Kim and Siegel, Mg_3AsN is the sole stable compound comprising magnesium, arsenic, and nitrogen,[14] and since arsenic begins to sublimate at 613 °C, the high-temperature synthesis reported by Chi *et al.* seems to be impractical for Mg_3AsN.

In our work, we present a successful method to synthesize Mg_3AsN *via* a mechanochemical route. The XRD measurements in Fig. 1a confirm the formation of cubic Mg_3AsN AP directly after ball milling at 300 rpm for 12 h or at 400 rpm for 3 h. The XRD patterns were compared with the computed structures reported by Xia *et al.*[5] and Goldmann *et al.*[6] The observed impurities in the spectrum of the sample milled at 400 rpm for 3 hours are attributed to zirconia contamination from the milling jar. In general, Mg_3AsN adopts a cubic AP structure with a space group of $Pm\bar{3}m$.[15,16] Furthermore, Farid *et al.* reported computational results, indicating that a stable orthorhombic phase with the space group of *Pnma* might also exist.[17,18] Our structure refinements (Fig. 1b) indicate the crystallization of Mg_3AsN directly after the ball milling in a cubic phase with a space group of $Pm\bar{3}m$, as depicted in Fig. 1c. The parameters used for structure refinement are shown in Table 1, while the resulting microstructure parameters are tabulated in Table 2 and will be discussed in detail later.

The SEM image (Fig. 1d) of the as-BM Mg_3AsN reveals that the crystal sizes range from 0.2 to 2.5 μm. Furthermore, EDS

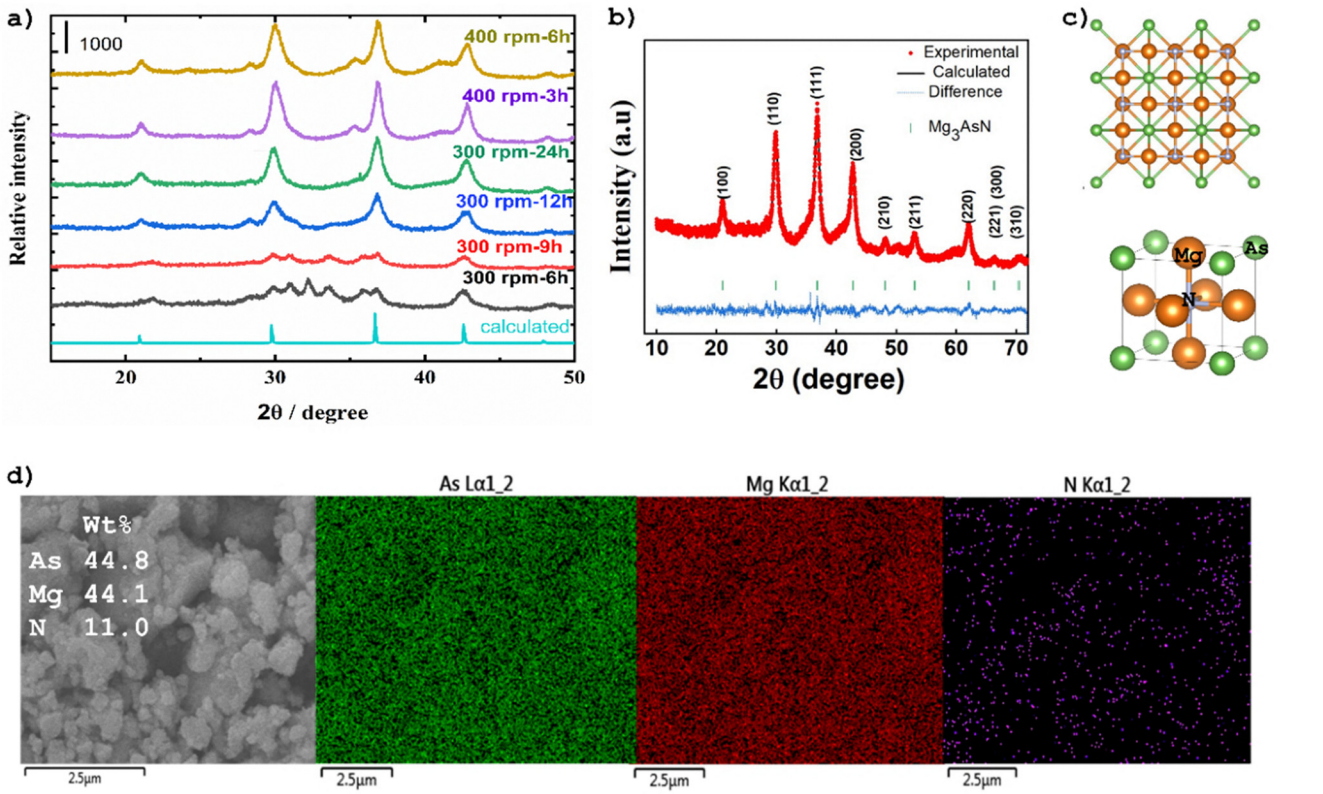

Fig. 1 (a) XRD patterns of the material with different ball-milling parameters, (b) Rietveld refinement of as-BM Mg_3AsN, (c) model of Mg_3AsN crystal showing its cubic structure, and (d) SEM image of the as-BM Mg_3AsN pellet, EDS analysis, and its corresponding elemental mapping.

elemental mapping (Fig. 1d) confirms the uniform distribution of Mg, As, and N. The computed chemical composition from EDS analysis yielded $Mg_{3.1}AsN_{1.3}$, thus confirming the successful synthesis of Mg_3AsN.

The air sensitivity of Mg_3AsN was assessed by exposing the material under ambient conditions, with XRD measurements taken over time (Fig. S2a). The results indicated that Mg_3AsN maintained its stability in air for up to 24 h without notable decomposition or phase change. Beyond this, the material gradually loses its crystallinity, becoming fully amorphous after one year.

For the solvent and moisture stability studies, Mg_3AsN was immersed in various polar (including H_2O) and nonpolar solvents for 24 h. The material was subsequently collected and dried, and then its XRD pattern was recorded. As shown in Fig. S2b, Mg_3AsN demonstrated poor stability in H_2O and other polar solvents compared to nonpolar solvents, indicating a high sensitivity to moisture relative to oxygen.

X-ray photoelectron spectroscopy (XPS) spectra were used to analyse the chemical composition of Mg_3AsN. Depth profiling using Ar^+ sputtering (2–20 minutes) was also carried out to study changes in the composition from the topmost surface layer to the surface-near bulk. As shown in Fig. S3a, the XPS survey spectrum of as-ball-milled Mg_3AsN confirms the presence of Mg, As, and N, along with small amounts of the commonly detected elements C and O. The deconvolution of the Mg-2p, As-3d, and N-1s peaks before and after 2–20 minutes of Ar^+ sputtering is shown in Fig. 2a and b. It should be mentioned that single peaks were used for the fit of the As-3d and Mg-2p peaks due to the relatively small spin–orbit-splitting of the two peaks (As-3d: Δ = 0.69 eV and Mg-2p: Δ = 0.28 eV). Initially, the deconvoluted XPS spectrum of Mg-2p (Fig. 2a) showed two peaks: the first and most significant peak at 49.3 eV corresponds to Mg bound to As and N in the antiperovskite (AP) framework. The second, lower-intensity peak at 50.5 eV can be attributed to surface oxidation and the formation of Mg–O/OH or to oxide impurities in Mg_3N_2.

The deconvolution of the As-3d spectrum (Fig. 2a) reveals three peaks at 39.7, 41.4, and 43.75 ± 0.1 eV, corresponding to arsenic in the oxidation states of −3 (AP), 0 (free metal or Mg–As alloy), and +3 (oxide), respectively. The peak at 43.75 ± 0.1 eV is primarily due to surface oxidation, as its intensity significantly decreases upon sputtering. Meanwhile, the peak at 39.7 ± 0.1 eV intensifies during sputtering. After 20 min of sputtering, the corrected intensity ratio (taking into account the atomic sensitivity factors) of the As-3d peak at 39.75 eV to the Mg-2p peak at 49.32 eV was 2.93 : 1, approaching the ratio of 3 : 1 of

Table 1 Refinement parameters for Mg_3AsN AP

Element	*X*	*Y*	*Z*	*B*	Occupancy	Multiplicity
Mg	0.00000	0.00000	0.50000	−5.953	0.063	3
As	0.50000	0.50000	0.50000	−7.981	0.023	1
N	0.00000	0.00000	0.00000	−8.890	0.021	1

Table 2 Micro-structure parameters from the refinements of as-BM and heat-treated Mg_3AsN

Structure/parameter	Lattice parameters	Density (g cm^{-3})	Cell volume (Å^3)	D (nm)	ε	R_p	R_{wp}	R_{exp}	χ^2
as-BM Mg_3AsN	4.2307	3.55	75.7275	14.1	6.67×10^{-3}	4.06	5.19	4.49	1.34
Mg_3AsN-500-12	4.2239	3.567	75.3608	31.4	1.64×10^{-3}	5.26	7.06	4.43	2.54
Mg_3AsN-600-12	4.2242	3.566	75.3781	25.4	2.33×10^{-3}	3.52	4.51	4.07	1.23
Mg_3AsN-700-12	4.2241	3.566	75.3702	38.4	0.87×10^{-3}	4.28	5.66	4.19	1.83

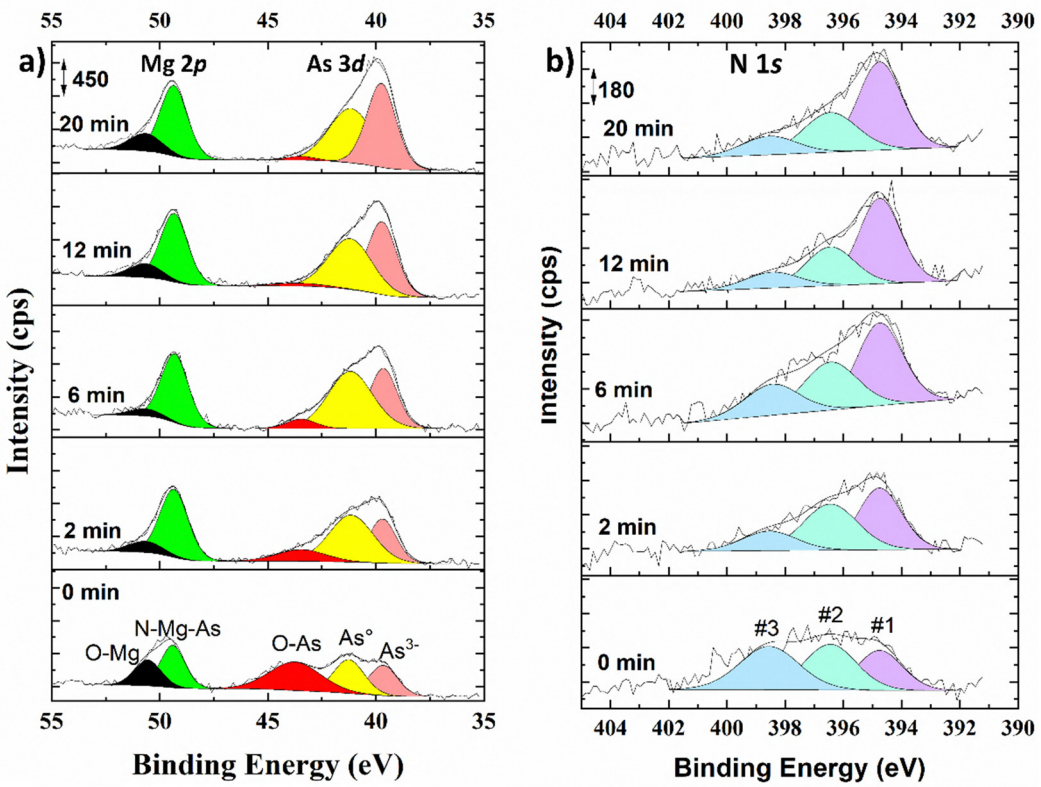

Fig. 2 Detailed XPS spectra in the (a) Mg-2p and As-3d and (b) N-1s regions of the as-ball milled Mg_3AsN at 400 rpm for 3 h (as BM Mg_3AsN). Spectra were recorded before and after Ar^+ sputtering for different periods indicated in the figure (0 min refers to the spectra of the sample before Ar^+ sputtering).

Mg_3AsN. Notably, the high-resolution N-1s spectrum (Fig. 2b) of the as-ball-milled Mg_3AsN before depth profiling exhibited three peaks at 395.2 eV, 396.4 eV, and 398.2 eV. The peak at 396.4 eV (N-1s#2), assigned to nitrides in the AP structure, showed the highest intensity among the three. The small peak at 398.2 eV (N-1s#3) has been reported for adsorbed N_2;[28] however, since its intensity did not diminish with Ar^+ sputtering, it is instead assigned to oxynitride species, where nitrogen is bound to metal, which is, in turn, bound to oxygen.[28] The formation of oxynitrides is attributed to impurities in the Mg_3N_2 precursor, which aligns with the Mg-2p peak at 50.6 ± 0.1 eV and the O-1s peak at 531.5 eV (see Fig. S3b).

The N-1s#1 peak, appearing at very low binding energy (395.2 ± 0.3 eV), has been previously reported and assigned to nitrogen atoms with a coordination number of less than four (under-coordinated N), bound to the metal,[29] or to the formation of defective N–N bonds, as described by Costales *et al.*[30] and Rosenberger *et al.*[31] Rosenberger *et al.* extensively discussed this phenomenon, attributing the formation of defective N–N bonds to the termination of a layer-by-layer deposition process, leading to an incomplete nitride layer. During the sputtering process, particularly at layer edges or column boundaries, incomplete layer formation increases the probability of partially broken nitrogen bonds, creating N–N defects.[31] Although this scenario does not directly apply to our synthesis protocol, a high degree of defect formation is still expected due to the high-energy ball-milling process. Therefore, the peak at 395.2 ± 0.3 eV is assigned to the formation of under-coordinated N in the APs. Depth profiling results further confirm this assignment, as the intensity of this peak increases while Ar^+ sputtering proceeds, indicating that sputtering creates further defects in the surface layer of the AP structure. Thus, one can conclude that, in this case, Ar^+ sputtering induces a high degree of surface defects, particularly nitrogen deficiency.

3.2 Electrochemical properties

To investigate the ionic and electronic properties of Mg_3AsN, electrochemical impedance spectra (EIS) of as-BM Mg_3AsN pellets sandwiched between different ion-blocking, half-blocking, and ion-non-blocking electrodes were recorded. The as-BM Mg_3AsN pellet sandwiched between two ion-blocking stainless steel electrodes (SS) showed very high interfacial resistance with a high degree of instabilities at room temperature (RT) and 40 °C (Fig. S4a) and a distorted semi-circle at higher temperatures (100 °C), as shown in Fig. S4b. Repeating the measurement after 24 h, we observed an increase in the resistance in the low-frequency region, indicating the reactivity of Mg_3AsN with stainless steel. Therefore, Au coated pellets were used as shown in Fig. 3a, and EIS measurements were recorded at different temperatures. No Warburg element was observed; instead, the low-frequency semicircle fully intersects the real axis of the Nyquist plot. This behavior indicates a non-blocking configuration, suggesting that the dominant physical process at low frequencies is the electronic conduction rather than double-layer capacitance associated with blocking behavior.[32] It is worth noting that the same results were obtained when Cu electrodes were used as ion-blocking electrodes (iBEs). As shown in Fig. 3b, the EIS spectra of as-BM Mg_3AsN sandwiched between two reversible Mg electrodes did not show any significant difference, but rather a slight distortion in the semi-circle due to the additional contact resistance in the presence of the Mg ion-non-blocking electrodes. This result refers to the mixed conductivity characteristics of the as-BM Mg_3AsN structure. The presence of only one distorted semi-circle instead of two well-resolved semi-circles indicates that both ionic and electronic conductivities are comparable. On the other hand, it is observed that the EIS spectra of the half ion-blocking configuration (half reversible, Au/Mg) and the ion-blocking cell configuration (Au/Au) at 100 °C are nearly identical. In an ion-blocking cell configuration, the iBEs are expected to impede the flow of ions, resulting in higher impedance. On the other hand, in a half-reversible cell configuration, where the RE allows for some ionic movement and electron transfer, the impedance would typically be lower. The fact that both configurations exhibit the same impedance suggests that the solid electrolyte is a mixed conductor.[33]

Herein, to fully characterize Mg_3AsN, deconvolution of the EIS spectra is mandatory. Two different experimental procedures were used to achieve this. First, the electronic conductivity was calculated from *DC* polarization of an Au|Mg_3AsN|Au cell at different voltages (0.5–3.0 V) (Fig. 3c), and then the steady-state current *vs.* the applied voltage could be plotted (Fig. 3d). The calculated total ion transport number of 0.077 confirms that the current passing through the material is predominantly carried by electrons, while the calculated electronic conductivity from Fig. 3d is found to be 4.9×10^{-8} S cm^{-1}.

Because of the low total ion transport number, it can be assumed that the ionic current gets mainly shunted by electronic current. To ascertain the ionic conductivity of the system, a specialized experimental setup was employed, featuring a cell equipped with two electrodes designed to impede the flow of electrons (Fig. 3e). These electrodes were crafted using

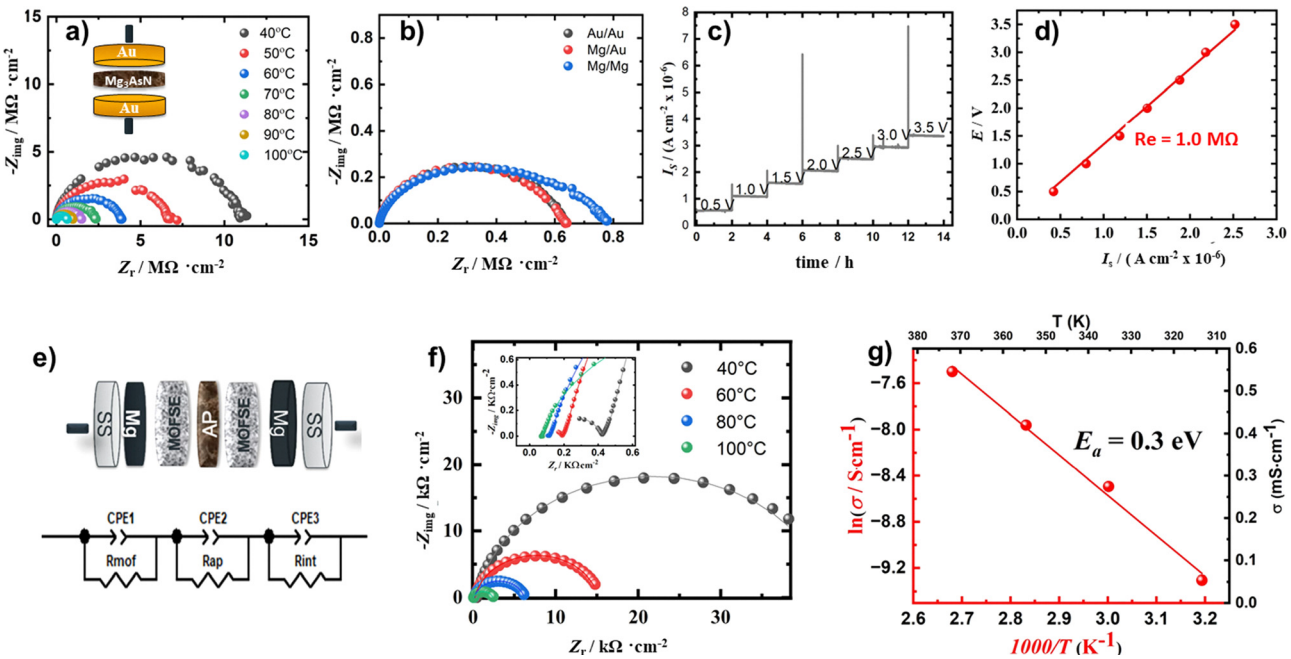

Fig. 3 (a) EIS spectra of Au|Mg_3AsN|Au measured at different temperatures, (b) the EIS spectra of as-BM Mg_3AsN measured between ion-blocking, half-blocking, and non-blocking electrodes, (c) chronoamperometry measurement of Au|Mg_3AsN|Au at different voltages, (d) recorded steady-state current *vs.* applied voltage, (e) schematic cell setup (top) and the equivalent circuit used to fit EIS results (bottom), (f) the EIS spectra of Mg|MOFsSE|Mg_3AsN|MOFsSE|Mg at different temperatures, and (g) Arrhenius plot (the ionic conductivity values were extracted from fitting of the EIS results shown in (f)) using the equivalent circuit shown in (e).

MOF-based semi-solid electrolytes (MOFsSE), known for their distinct properties as pure ion conductors.[34,35]

This method has previously been reported as an effective way to separate ionic and electronic conductivities using either polymeric solid electrolytes (SEs)[32] or MOF-based SEs.[26] Both iBEs and REs (such as Mg) can be employed. In this regard, Janek *et al.*[26] and Sakamoto *et al.*[32] reported iBE|eBE|SE|eBE|iBE and RE|eBE|SE|eBE|RE as the electron blocking cell configurations, respectively. In our work, the cell configuration Mg|eBE|SE|eBE|Mg was used. As shown in Fig. 3f, the EIS spectra of Mg|MOFsSE|Mg_3AsN|MOFsSE|Mg were measured at different temperatures. Before this experiment, EIS spectra of the iBE|MOFsSE|iBE cell were measured over the same temperature range to determine the exact ionic conductivity of the MOFsSE. At 100 °C, MOFsSE showed a bulk resistance of 14.6 Ω.[24] To extract the precise ionic resistance within the system, the EIS measurement shown in Fig. 3f was fitted with the equivalent circuit shown in Fig. 3e, where R_{mof} is the resistance from the MOFsSE, R_{ap} is the resistance of the AP, and R_{int} is the resistance of the interface. Because the MOFsSE blocks the flow of electrons, the charge transport must be related to ions. That is why R_{ap} can be assumed to be the bulk resistance (R_b) of the AP. Modeling using the ZView software yielded ionic resistance and conductivity of the AP at a high degree of precision, providing an ionic conductivity of 5.54×10^{-4} S cm^{-1} at 100 °C. The activation energy for Mg^{2+} migration (E_a) was determined from the Arrhenius plot (Fig. 3g) and found to be 0.3 eV, which is consistent with other Mg-ion SEs.[36]

3.3 Effect of post-heat treatment

To enhance the crystallinity of Mg_3AsN, post-heat treatment experiments were conducted at different temperatures and durations. The XRD analysis of the heat-treated pellets (Fig. 4a) reveals that the material undergoes decomposition at 800 °C, resulting in the formation of an Mg_3As_2 alloy. At 700 °C, the XRD pattern does not exhibit any impurities; however,

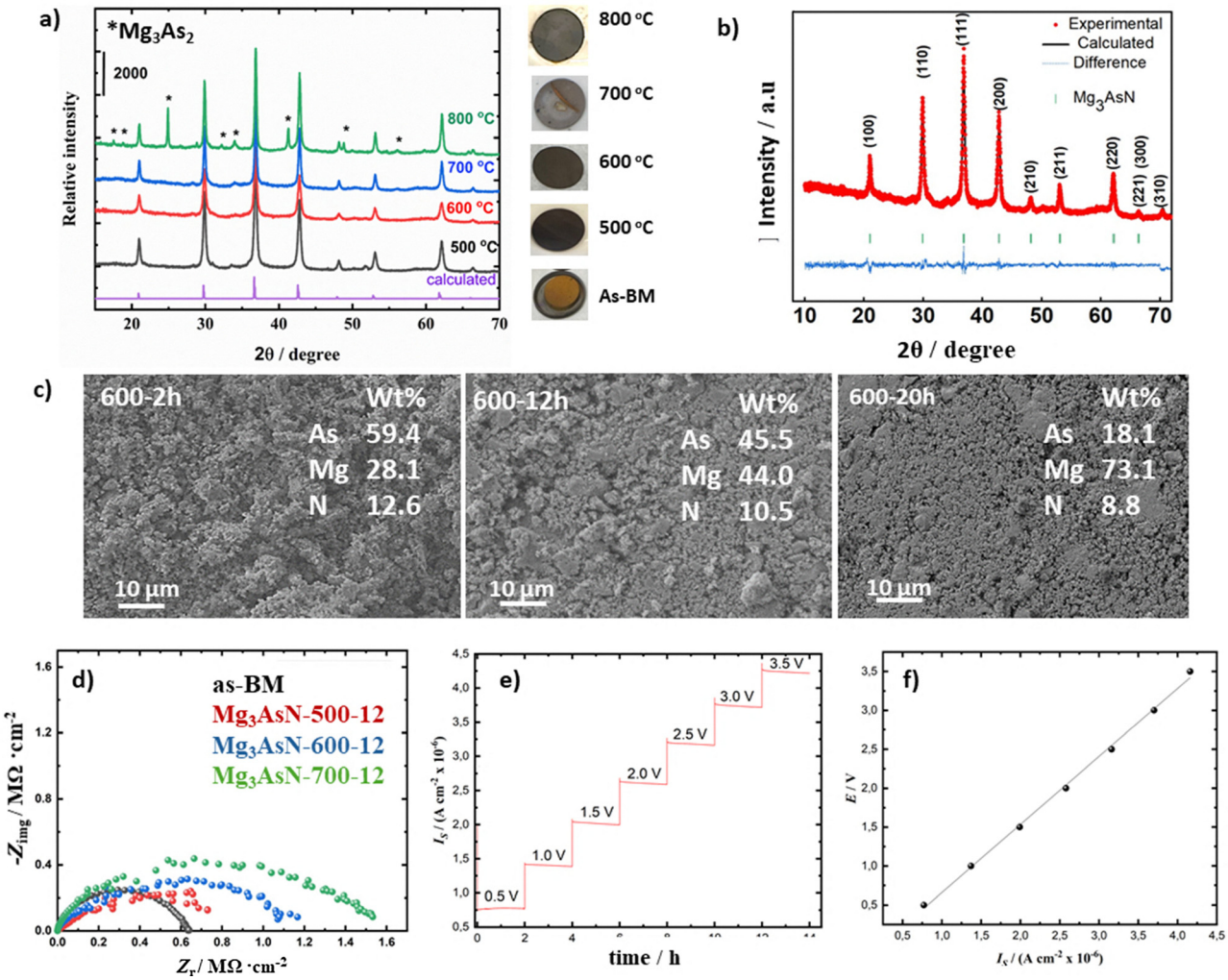

Fig. 4 (a) XRD and light images of Mg_3AsN after heating at different temperatures for 12 h, (b) XRD pattern and Rietveld refinements of the heat-treated Mg_3AsN at 600 °C for 12 h, (c) SEM images and elemental composition of the heat-treated Mg_3AsN at 600 °C for different times, (d) EIS spectra of the Au/Mg_3AsN/Au cell with the heat-treated material, (e) chronoamperometry measurement of the Au/Mg_3AsN/Au cell with heat-treated Mg_3AsN at 600 °C for 12 h, and (f) recorded steady-state current *vs.* applied voltage of the CA measurement.

surface segregation and an inhomogeneous color change were noticed on the pellet's surface. Consequently, a temperature of 600 °C was selected for subsequent investigations. Fig. 4b shows a Rietveld refinement plot for heat-treated Mg_3AsN at 600 °C for 12 h.

The refinement shows that the heat treatment did not change the cubic structure of the crystal. The Williamson–Hall plot used to calculate the crystallite size and the lattice macrostrain parameter is shown in Fig. S5a. It is observed that all samples showed a positive slope, indicating a tensile strain. The as-BM sample exhibits a crystallite size of 14.1 nm and a high lattice strain of 6.67×10^{-3} due to the high concentration of defects created by ball milling as previously discussed in the XPS results. Upon heat treatment, the crystallite size increases resulting in a decrease in the density of the grain boundaries and consequently a decrease in microstructure strain, indicating a lattice relaxation. Moreover, the lattice parameters slightly decreased with heat treatment, resulting in a slight decrease in the cell volume.

EDS mapping results shown in Fig. S5b revealed that post-heat treatment at 600 °C for 12 h did not affect the elemental composition of the material. Regarding the sintering time, SEM imaging (Fig. 4c) demonstrates that increasing the duration leads to increased pellet compactness and a more homogeneous surface; however, a significant decrease in the arsenic composition was observed after heating at 600 °C for 20 h. Therefore, 12 h was selected as an optimum heat treatment duration. The XPS survey spectrum of heat-treated Mg_3AsN-600-12 confirmed the structural composition (Fig. S6a). Deconvolution of the Mg-2p, As-3d, and N-1s spectra did not show significant differences compared to as-ball-milled (BM) Mg_3AsN. However, after heat treatment, a Mg-rich surface formed, leading to a lower surface content of As relative to Mg. Most of the As-3d signal was associated with As in the AP structure, as shown in Fig. S6b. Upon sputtering, the As-3d peak intensity increased relative to the Mg peak until a ratio of 3.24 : 1 Mg-2p : As-3d was reached after 20 minutes of Ar^+ sputtering. On the other hand, after sintering, the N-1s#1 peak at 394.8 eV (Fig. S6c) exhibited very low intensity compared to the as-BM spectrum, further supporting the correlation of this peak with defected structures. Heat treatment stabilized the structure, transforming metastable states produced during ball milling into a highly crystalline, stable phase while reducing defect concentrations. Upon Ar^+ sputtering, the intensity of this peak increased due to the reformation of surface defects, as previously discussed. Overall, both as-BM and sintered samples exhibited lower surface nitrogen content than expected, indicating the formation of a nitrogen-deficient surface. In contrast, bulk analysis *via* EDS revealed a relatively higher nitrogen content, confirming that nitrogen deficiency is primarily a surface phenomenon.

Employing EIS, the effects of heat-treatment temperature on the ionic and electronic resistance of Mg_3AsN were scrutinized. The Nyquist plots in Fig. 4d revealed an increase in the high-frequency region, indicative of elevated electronic resistance. This effect intensified with higher sintering temperatures. However, due to the significant surface segregation observed at 700 °C, subsequent experiments were conducted with materials heated at 600 °C for 12 h.

The total ionic transport numbers of the samples heated at 600 °C for 12 h were calculated from chronoamperometry (CA) measurements at 0.5 V until the steady-state current was achieved, as shown in Fig. 4e. An improved total ion transport number, $t_{ion} = 0.615$, could be achieved. An electronic conductivity value of $\sigma_{el} = 6.87 \times 10^{-8}$ S cm^{-1} was obtained for the material heated at 600 °C (Fig. 4f), which is nearly the same as in as-BM Mg_3AsN despite the improved t_{ion}. This could be due to the higher interfacial resistance associated with the rough surface of the as-BM material, as will be discussed later. These findings indicate improved ionic diffusion and consequently total transport number after high-temperature sintering of Mg_3AsN. Similarly, as in the case of the as-BM sample, MOFsSE buffering pellets were used to block the electronic motion in order to deconvolute the ionic conductivity value. As shown in Fig. S7, the calculated ionic conductivity at 100 °C was found to be $\sigma_{ion} = 2 \times 10^{-4}$ S cm^{-1}. Since the electronic conductivity values of the as-BM Mg_3AsN calculated from DC measurements do not match with the total transport number, a contribution from interfacial and grain boundary resistances is highly predicted. This was also observed in the appearance of scattered points in the EIS plots, in particular, at relatively low temperatures. Therefore, hot-pressing was employed in order to smooth the pellet's surface and to densify it. Both as-BM Mg_3AsN and the heat-treated one, Mg_3AsN-600-12, were hot-pressed at 100 °C using the same pressure and time as in the cold-pressed samples. The powder was heated up to 100 °C inside the pressing mould and then kept at this temperature for 10 min before applying the pressure. The cells were sintered at 100 °C for three days before EIS measurements. As shown in Fig. S8a, the EIS plots of hot-pressed BM Mg_3AsN showed much lower total resistance compared to the cold-pressed pellets, indicating an improved interface with smoother connection between the electrolyte and the electrodes. However, in the case of the heat-treated one (Fig. S8b), there is no significant decrease in the total impedance, indicating similar electronic conductivity compared to the cold-pressed pellet. DC polarizations were recorded at different applied voltages to calculate the electronic conductivity at 100 °C for both samples. As shown in Fig. S8c–e, the calculated electronic conductivity after minimizing the interfacial resistance was found to be 1.5×10^{-6} S cm^{-1} and 2.4×10^{-8} S cm^{-1} for as-BM and Mg_3AsN-600-12, respectively. One can conclude that the main effect of the heat treatment is related to improving the interfacial and grain boundary resistances and minimizing the electronic conductivity. Although the enhanced interface upon hot-pressing allowed for a more precise electronic conductivity calculation, the experiment using a cell where the Mg_3AsN pellet is sandwiched between two electron-blocking layers detected a decreased ionic conductivity, as shown in Fig. S9. This could be due to the significant reduction of the porosity after hot-pressing, which hindered the ionic diffusion in Mg_3AsN.

3.4 Approaches to shield the electronic conductivity of Mg_3AsN

From the previously discussed results, one can conclude that Mg_3AsN exhibits relatively high ionic conductivity; however, its

application as a solid electrolyte is hindered by its significant electronic conductivity contribution. The structure and chemical manipulation approaches shown here were not enough to significantly minimize its electronic conductivity, which then resulted in a short circuit in the Mg|Mg cell. To address this issue, we tested different strategies to shield the electronic conductivity of Mg_3AsN while allowing the ions to flow.

The first approach involved using a buffering electrolyte, MOFsSE, to block electronic motion and prevent short circuits. In this case, the MOFsSE/Mg_3AsN/MOFsSE composite was used as a solid electrolyte, and its Mg deposition/stripping profile was then investigated. Herein, the ionic conductivity of this combined composite will be mainly governed by the ionic conductivity of Mg_3AsN, offering a total ionic conductivity of 0.094 mS cm^{-1} at 40 °C which increased to 0.76 m S cm^{-1} at 100 °C.

As shown in Fig. 5a, the Mg|MOFsSE|Mg_3AsN|MOFsSE|Mg cell was successfully cycled at room temperature under a DC of ±0.01 mA for more than 90 cycles. Initially, Mg deposition occurred at −0.1 V, while Mg dissolution took place at approximately 0.03 V. However, the overpotential gradually increased with cycling, reaching −2 V and 1.9 V, respectively. This increase could be due to the accumulation of oxygen on the surface of the Mg anode, which is difficult to remove from the Mg anode surface, as reported by Janek *et al.*[34] This could

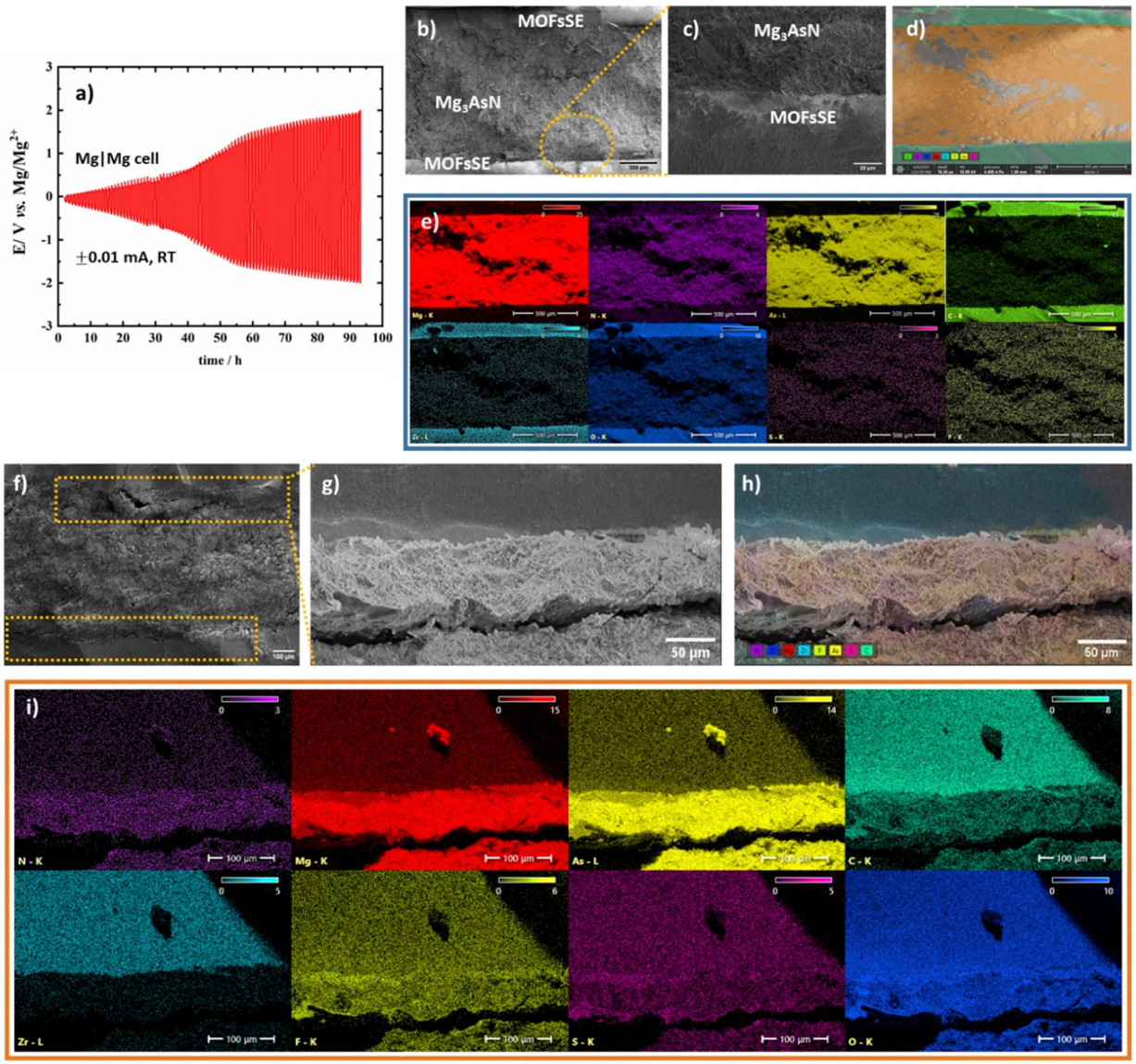

Fig. 5 (a) GCD cycling of Mg|MOFsSE|Mg_3AsN|MOFsSE|Mg at RT and ±0.01 mA; (b) cross-sectional SEM micrograph of the MOFsSE|Mg_3AsN|MOFsSE pellet before cycling; (c) cross-sectional SEM micrograph of higher magnification, (d) the corresponding overall mapping image, and (e) the corresponding EDS elemental mapping images; (f) cross-sectional SEM micrograph of the MOFsSE|Mg_3AsN|MOFsSE pellet after GCD cycling; and (g) cross-sectional SEM micrograph of higher magnification, (h) the corresponding overall mapping image, and (i) the corresponding EDS elemental mapping analysis.

certainly be one of the reasons, but it is not the main reason since the overpotential increase in cycling has not been observed in the initial cycle. Another significant reason is the partial decomposition of the $TFSI^-$ anions present in the MOFsSE layer during cycling, as we reported in our previous work.[37–39] The cross-sectional SEM image was recorded after GDC to investigate other reasons for further increasing the overpotential upon cycling, such as the loss of the AP/MOFsSE contact or the formation of cracks. As depicted in Fig. 5b–d, the Mg_3AsN|MOFsSE contact before cycling is highly compact, and no delamination or cracks were observed. The elemental mapping shown in Fig. 5e confirmed the chemical composition of

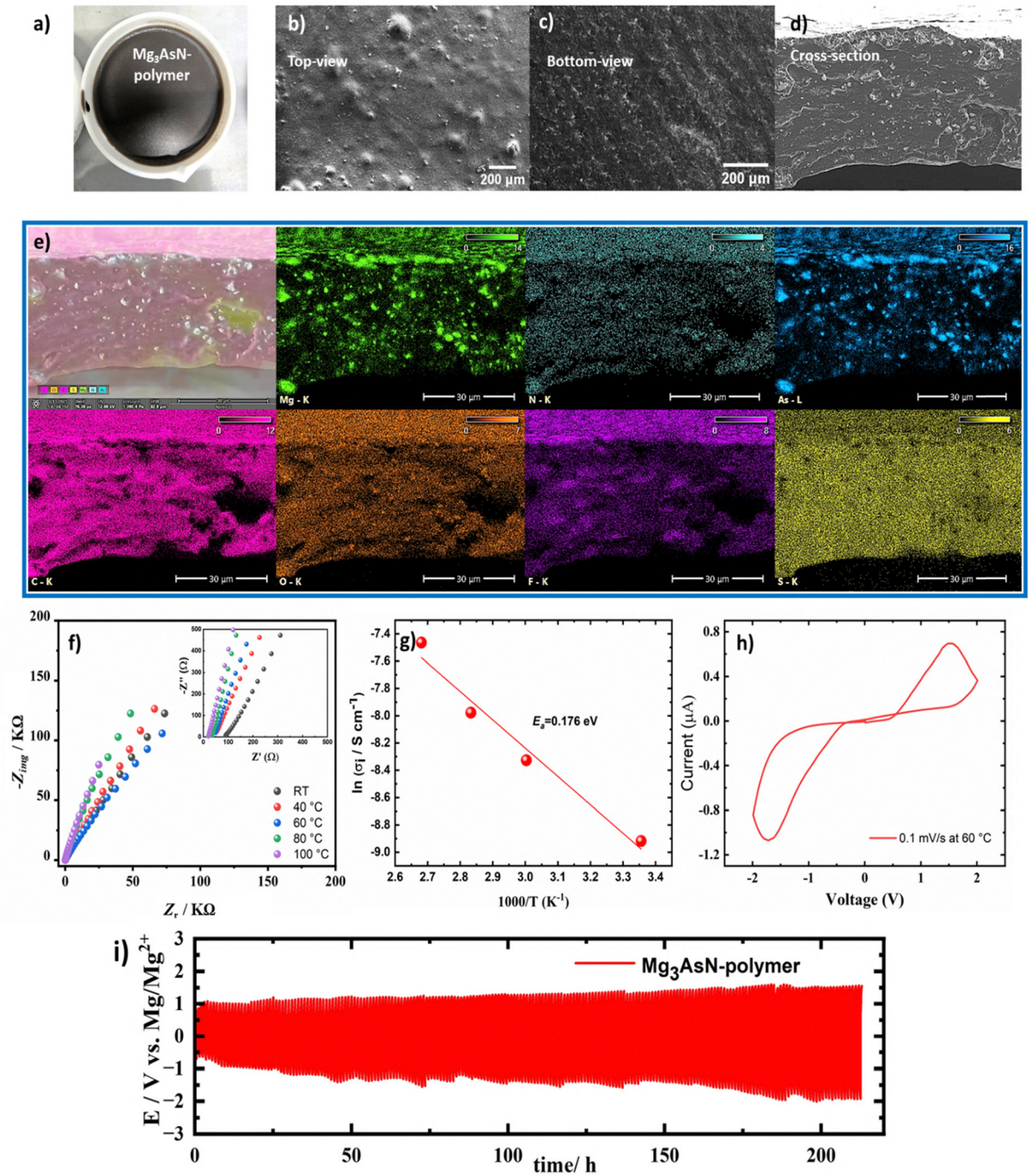

Fig. 6 (a) A light photograph of the Mg_3AsN–polymer membrane; (b) top-view SEM micrograph of the Mg_3AsN–polymer membrane, (c) the corresponding bottom-view SEM micrograph, (d) the corresponding cross-sectional SEM micrograph, and (e) the corresponding EDS mapping analysis; (f) Nyquist plot of the SS|Mg_3AsN–polymer|SS cell at different temperatures and (g) the corresponding Arrhenius plot (ionic conductivity values were calculated from the bulk resistances extracted from (f)); (h) CV at 60 °C of Mg|Mg_3AsN–polymer|Mg showing the successful Mg deposition and dissolution processes; and (i) GCD cycling of the Mg_3AsN–polymer membrane at 2 µA cm^{-2} measured at 60 °C.

each layer. While the layers are clearly discernible for the most elements (Mg, As and N in Mg_3AsN and C, O and Zr in MOFsSE), the elemental mapping of F and S (coming from $TFSI^-$ in MOFsSE) showed a homogeneous distribution in all layers, indicating free migration of $TFSI^-$ anions from the MOFsSE layer through the Mg_3AsN layer. After cycling, surface delamination of Mg_3AsN from the MOFsSE layer and cracks in both layers (Fig. 5f–h) throughout the pellet were observed. Therefore, the increase in overpotential is mainly due to the loss of contact between MOFsSE and the Mg_3AsN layer. Although this strategy effectively shields the electronic contribution of Mg_3AsN, further investigations and optimizations are required to address the loss of contact with prolonged cycling. Perhaps a very thin layer of ionic liquid between the layers can improve the interface, minimize the stress, and consequently prevent crack formation and delamination.

Since the layering concept showed a relatively high overpotential upon cycling, the second approach involved embedding Mg_3AsN in a polymeric matrix to suppress electronic conductivity and to minimize the Mg^{2+} ion diffusion pathway. This was achieved by incorporating Mg_3AsN as a magnesium-ion source in a co-polymer composed of PVA, PEGDA, PVDF-HFP, and EMIM-TFSI IL as described in the Experimental section. As shown in Fig. 6a–e, Mg_3AsN was successfully dispersed in the polymer matrix and the cross-sectional image and ion mapping proved the homogeneous distribution. However, we noticed that AP particles were slightly concentrated at the bottom of the membrane compared to the top. Optimizing the composite parameters, such as the composition and synthesis conditions, might improve this. XRD patterns of the membrane showed the presence of the main diffraction peaks of Mg_3AsN, indicating its stability in the polymer matrix, as shown in Fig. S10.

Integrating Mg_3AsN into the polymer matrix significantly enhanced the total ionic conductivity while effectively suppressing its electronic conductivity. The Nyquist plot of the SS|Mg_3AsN–polymer|SS shown in Fig. 6f exhibited a spike in the low-frequency region, and the total impedance was reduced compared to the case where the MOFsSE was used as a buffering layer. This method aimed to shorten the diffusion pathway by minimizing the number of layers required for cell assembly, thereby improving ionic conductivity and reducing interfacial resistance. As shown in Fig. 6g, a RT ionic conductivity of 0.134 mS cm^{-1} and a diffusion barrier as low as 0.174 eV were obtained for the Mg_3AsN–polymer composite, indicating the efficiency of the proposed approach in improving the total ion diffusion. Moreover, the cyclic voltammogram (CV) of the Mg|Mg_3AsN–polymer|Mg cell at 0.1 mV s^{-1} and 60 °C shown in Fig. 6h showed a successful Mg deposition and dissolution at –1.6 and +1.4 V *vs.* Mg/Mg^{2+}, respectively. In addition to the problems associated with the Mg anode, as we discussed before, this high overpotential could also be due to the difference in the concentration of Mg^{2+} ions at the top and bottom of the membrane. Additionally, the interfacial stability of the Mg_3AsN–polymer membrane was assessed by an aging test of the Mg|Mg_3AsN–polymer|Mg cell, which was conducted through EIS investigations for 6 days. As shown in Fig. S11, no degradation or change in the interfacial resistance was observed, indicating the high interfacial stability of the polymer composite against the Mg electrode. GCD cycling of the Mg|Mg_3AsN–polymer|Mg cell at 2 μA cm^{-2} shown in Fig. 6i revealed a reversible and relatively stable Mg deposition/stripping process for more than 200 cycles, indicating the successful shielding of the electronic conductivity of Mg_3AsN, making it a promising approach to unlock the full potential of antiperovskites as ionic conductors for multivalent batteries.

4. Conclusions

In conclusion, the experimental investigations presented in this study align with the previous theoretical predictions concerning the electronic properties of the Mg_3AsN anti-perovskite. The as-ball-milled Mg_3AsN AP acts as a mixed conductor, exhibiting ionic and electronic conductivities of 5.5×10^{-4} and 1.5×10^{-6} S cm^{-1} (at 100 °C) after reducing the grain boundary and interfacial resistances. Heat treatment reduced the electronic conductivity to 5×10^{-8} S cm^{-1}. It enhanced Mg^{2+} ion diffusion and increased the total transport number from 0.07 for the as-BM Mg_3AsN to 0.615 after heat treatment at 600 °C for 12 h.

To emphasize Mg_3AsN's potential as a Mg-ion conductor, we compared it with other Mg-ion conductors. As shown in Table S1, compared to other inorganic solid-electrolytes, Mg_3AsN exhibits comparable ionic conductivity while offering significant advantages, including a simpler synthesis process, sufficient air stability for handling in a dry room, and excellent compatibility with our electron-conductivity shielding methodologies. In addition, the high flexibility of the structure towards structural manipulation is highly predicted to tune its physicochemical properties.

Surface analysis by XPS revealed that the as-BM Mg_3AsN exhibited lower surface nitrogen content than anticipated, indicating the formation of a nitrogen-deficient surface. Conversely, bulk analysis by EDS revealed a relatively higher nitrogen content, confirming that the nitrogen deficiency is primarily a surface phenomenon. Furthermore, we have demonstrated two promising strategies to reduce the electronic conductivity of Mg_3AsN either by employing electron-blocking MOFsSE layers or by embedding Mg_3AsN particles in a polymeric matrix. The first approach achieved successful galvanostatic cycling at room temperature under a direct current (DC) of ±0.01 mA for over 90 cycles. Mg deposition initially occurred at −0.1 V, while Mg dissolution took place at approximately 0.03 V. However, the overpotential gradually increased with cycling, reaching −2 V and 1.9 V, respectively. This is attributed to delamination and microcrack formation during cycling, as observed in post-mortem cross-sectional SEM analysis. Meanwhile, the second approach resulted in a highly stable Mg_3AsN free-standing polymer with an ionic conductivity of 0.134 mS cm^{-1}, an activation energy of diffusion as low as E_a = 0.174 eV, and a relatively stable galvanostatic

deposition/stripping cycling for more than 200 cycles. Further investigations are underway to improve both strategies and fully reveal their potential.

Author contributions

PH, IVM, HKH, and OE conducted the experiments, PH and HKH analysed and visualized the data. TD performed and analysed the XPS results. HKH conceptualized the work, contributed to the data validation, and designed the experiments. TJ funded the work and contributed to the work's conceptualization and data validation. PH and HKH wrote the initial draft. TJ and HKH supervised the work.

Conflicts of interest

There are no conflicts to declare.

Data availability

All data supporting this article have been included as part of the supplementary information (SI) of this study and are available from the authors upon reasonable request. Supplementary information: Results of the unsuccessful attempts to synthesize Mg_3AsN by high-temperature synthesis, air, and moisture stability of Mg_3AsN. XPS survey of as ball-milled Mg_3AsN, XPS survey and high resolution peak analyses of annealed Mg_3AsN, Williamson–Hall plots of as-BM and heat-treated Mg_3AsN as well as the EDS analysis of the heat-treated Mg_3AsN, Nyquist plots of Mg_3AsN against stainless steel ion blocking electrodes, Nyquist block of the electron blocking configurations, Mg|MOFsSE|Mg_3AsN-600-12|MOFsSE|Mg, at different temperatures as well as the corresponding Arrhenius plot, the effect of hot-pressing on the ionic and electronic properties of as-BM Mg_3AsN and heat-treated sample, Nyquist plots of the electron blocking configurations of hot-pressed Mg_3AsN pellet, Mg|MOFsSE|as-BM Mg_3AsN hot-pressed|MOFsSE|Mg at different temperatures and its corresponding Arrhenius plot, XRD pattern of Mg_3AsN-polymer membrane, interfacial stability of Mg_3AsN-polymer membrane against Mg electrodes, and Comparative table comparing Mg_3AsN to some reported Mg-ion conductors. See DOI: **https://doi.org/10.1039/d5mh01361e**.

Acknowledgements

The authors gratefully acknowledge funding from the Deutsche Forschungsgemeinschaft (DFG) through the priority program SPP 2248 Polymer-based Batteries (Project ID 441209207) and through the individual project with ID 501805371, and through Project ID 390874152 (POLiS Cluster of Excellence).

References

1 R. Mohtadi and F. Mizuno, *J. Nanotechnol.*, 2014, **5**, 1291–1311.
2 G. Olabi, Q. Abbas, P. A. Shinde and M. A. Abdelkareem, *Energy*, 2023, **266**, 126408.
3 P. C. Tsai, S. Mair, J. Smith, D. M. Halat, P. H. Chien, K. Kim, D. Zhang, Y. Li, L. Yin, J. Liu, S. H. Lapidus, J. A. Reimer, N. P. Balsara, D. J. Siegel and Y. M. Chiang, *Adv. Energy Mater.*, 2023, **13**, 2203284.
4 Y. Zhan, W. Zhang, B. Lei, H. Liu and W. Li, *Front. Chem.*, 2020, **8**, 125.
5 W. Xia, Y. Zhao, F. Zhao, K. Adair, R. Zhao, S. Li, R. Zou, Y. Zhao and X. Sun, *Chem. Rev.*, 2022, **122**, 3763–3819.
6 B. A. Goldmann, M. J. Clarke, J. A. Dawson and M. S. Islam, *J. Mater. Chem. A*, 2022, **10**, 2249–2255.
7 M. Bilal, S. Jalali-Asadabadi, R. Ahmad and I. Ahmad, *J. Chem.*, 2015, **2015**, 495131.
8 X. Lü, J. W. Howard, A. Chen, J. Zhu, S. Li, G. Wu, P. Dowden, H. Xu, Y. Zhao and Q. Jia, *Adv. Sci.*, 2016, **3**, 1500359.
9 Y. Zhao and L. L. Daemen, *J. Am. Chem. Soc.*, 2012, **134**, 15042–15047.
10 Y. Sun, Y. Wang, X. Liang, Y. Xia, L. Peng, H. Jia, H. Li, L. Bai, J. Feng, H. Jiang and J. Xie, *J. Am. Chem. Soc.*, 2019, **141**, 5640–5644.
11 Y. Li, W. Zhou, S. Xin, S. Li, J. Zhu, L. Xujie, Z. Cui, Q. Jia, J. Zhou, Y. Zhao and J. B. Goodenough, *Angew. Chem., Int. Ed.*, 2016, **55**, 9965–9968.
12 M. H. Braga, J. A. Ferreira, V. Stockhausen, J. E. Oliveira and A. El-Azab, *J. Mater. Chem. A*, 2014, **2**, 5470–5480.
13 C. C. Dutra and J. A. Dawson, *J. Phys. Chem. C*, 2023, **127**, 18256–18270.
14 K. Kim and D. J. Siegel, *Chem. Mat.*, 2021, **33**, 2187–2197.
15 Y. Mochizuki, H. J. Sung, A. Takahashi, Y. Kumagai and F. Oba, *Phys. Rev. Mater.*, 2020, **4**, 1–7.
16 Z. Gao, W. Wang, B. Chen Li, L. Sun and F. Wang, *J. Supercond. Nov. Magn.*, 2022, **35**, 3277–3290.
17 H. M. Tahir Farid, A. Mera, T. I. Al-Muhimeed, A. A. AlObaid, H. Albalawi, H. H. Hegazy, S. R. Ejaz, R. Y. Khosa, S. Mehmood and Z. Ali, *J. Mater. Res. Technol.*, 2021, **13**, 1485–1495.
18 X. Li, Y. Zhang, W. Kang, Z. Yan, Y. Shen and J. Huo, *Comput. Mater. Sci.*, 2023, **225**, 112188.
19 C. M. I. Okoye, *Mat. Sci. Eng. B*, 2006, **130**, 101–107.
20 I. R. Shein and A. L. Ivanovskii, *J. Solid State Chem.*, 2004, **177**, 61–64.
21 A. Bouhemadou and R. Khenata, *Comput. Mater. Sci.*, 2007, **39**, 803–807.
22 E. Oyeniyi, *Solid State Commun.*, 2022, **325**, 114927.
23 E. O. Chi, W. S. Kim, N. H. Hur and D. Jung, *Solid State Commun.*, 2002, **121**, 309–312.
24 P. Hoffmann, O. El-Khafif, T. Jacob and H. K. Hassan, The Influence of Metal–Organic Framework/Ionic Liquid Electrolyte Microstructure on Ionic Conductivity and Performance in Rechargeable Magnesium Batteries, Under publication.
25 L. B. Mccusker, R. B. Von Dreele, D. E. Cox, D. Louër and P. Scardi, *J. Appl. Crystallogr.*, 1999, **32**, 36–50.
26 C. Glaser, Z. Wei, S. Indris, P. Klement, S. Chatterjee, H. Ehrenberg, Z. Zhao-Karger, M. Rohnke and J. Janek, *Adv. Energy Mater.*, 2023, **13**, 202301980.

27 N. Doppelhammer, N. Pellens, C. E. A. Kirschhock, B. Jakoby and E. K. Reichel, *IEEE Sens. J.*, 2021, **21**, 9636–9641.
28 M. I. A. Samad, M. M. Noor, N. Nayan, A. S. A. Bakar, M. Mansor, A. W. M. Zuhdi, A. A. Hamzah and R. Latif, *Scr. Mater.*, 2023, **226**, 115228.
29 F. Chale-Lara, M. Zapata-Torres, F. Caballero-Briones, W. De la Cruz, N. Cruz González, C. Huerta-Escamilla and M. H. Farías, *Rev. Mex. Fis.*, 2019, **65**, 345–350.
30 A. Costales, M. A. Blanco, Á. Martín Pendás, A. K. Kandalam and R. Pandey, *J. Am. Chem. Soc.*, 2002, **124**, 4116–4123.
31 L. Rosenberger, R. Baird, E. McCullen, G. Auner and G. Shreve, *Surf. Interface Anal.*, 2008, **40**, 1254–1261.
32 M. J. Wang, J. B. Wolfenstine and J. Sakamoto, *Adv. Funct. Mater.*, 2020, **30**, 201909140.
33 A. E. Bumberger, A. Nenning and J. Fleig, *Phys. Chem. Chem. Phys.*, 2024, **26**, 15068–15089.
34 Z. Wei, R. Maile, L. M. Riegger, M. Rohnke, K. Müller-Buschbaum and J. Janek, *Batteries Supercaps*, 2022, **5**, e202200318.
35 Y. Yoshida, T. Yamada, Y. Jing, T. Toyao, K. I. Shimizu and M. Sadakiyo, *J. Am. Chem. Soc.*, 2022, **144**(19), 8669–8675.
36 P. W. Jaschin, Y. Gao, Y. Li and S. H. Bo, *J. Mater. Chem. A*, 2020, **8**, 2875–2897.
37 H. K. Hassan, P. Hoffmann and T. Jacob, *ChemSusChem*, 2024, **17**, e202301362.
38 O. W. Elkhafif, H. K. Hassan, M. U. Ceblin, A. Farkas and T. Jacob, *ChemSusChem*, 2023, **16**, e202300421.
39 H. K. Hassan, A. Farkas, A. Varzi and T. Jacob, *Batteries Supercaps*, 2022, **5**, e202200260.